Supplemantary Information

Exfoliating spent cathode materials with robust interlayer interactions into thin nanosheets for oxygen evolution reaction

Cheng Huang[a], Hong Lv[a], Zeheng Yang[a*], Cheng Lian[b*], Jianglong Du[b], Guoqiang Liu[a], Weijian Tang[a], Zhengjie Xu[a], Ziwei Chi[a], Honglai Liu[b], Haijian Huang[a*], Weixin Zhang[a*]

[a] School of Chemistry and Chemical Engineering, Anhui Key Laboratory of Controllable Chemical Reaction and Material Chemical Engineering, Hefei University of Technology, Hefei, 230009, P. R. China

[b] State Key Laboratory of Chemical Engineering, Shanghai Engineering Research Center of Hierarchical Nanomaterials, Frontiers Science Center for Materiobiology and Dynamic Chemistry, School of Chemistry and Molecular Engineering, East China University of Science and Technology, Shanghai 200237, P. R. China

*Corresponding authors: zehengyang@hfut.edu.cn, wxzhang@hfut.edu.cn, haijian.huang@hfut.edu.cn, liancheng@ecust.edu.cn
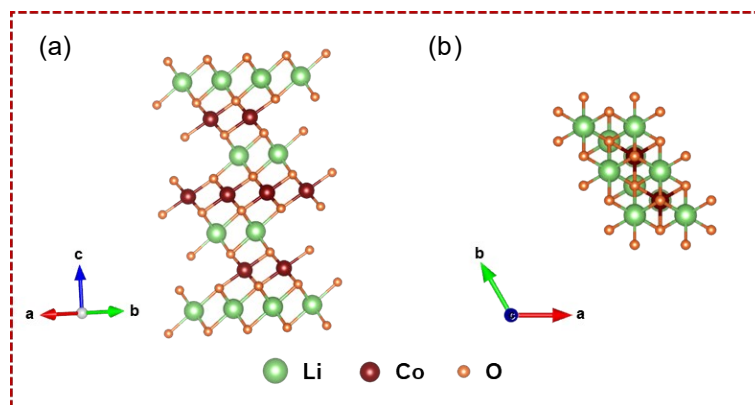
Fig. S1 Side view (a) and top view (b) of the bulk $LiCoO_2$ structure.

The binding energy of Li-O in $LiCoO_2$ was calculated according to the equation:

$\Delta E = E_{Li\text{-}vacancy} + E_{Li} - E_{total}$, which was determined to be 2.90 eV per atom.
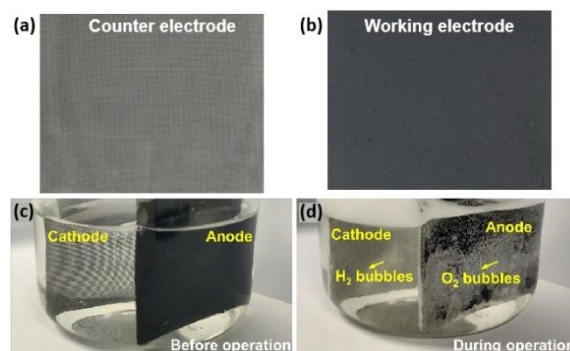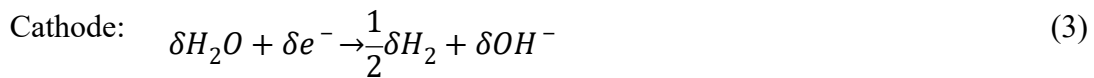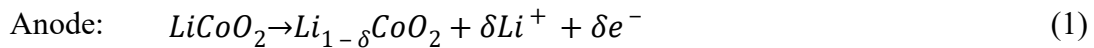

Fig. S2 Photograph of the pure titanium mesh (a, counter electrode) and the titanium mesh with the electrode materials casted (b, working electrode). The coating area is about 4 cm × 5 cm. Photos of the electrolytic bath (c) before and (d) during operation.

The LiCoO$_2$ powders and polyvinylidene fluoride (PVDF) were mixed with a mass ratio of 30: 1 in the N-methyl-2-pyrrolidone (NMP) solvent first. The obtained sticky slurry was then casted onto titanium meshes (Fig. S2a) and dried at 80 °C in air for 1 h to obtain the working electrode (Fig. S2b). The electrochemical treatment for bulk LiCoO$_2$ is performed in a two-electrode system (Fig. S2c) with sodium dodecylbenzene sulfonate (SDBS) aqueous solution employed as the electrolyte. The production of O$_2$ bubbles can be clearly observed at the anode side (Fig. S2d). The erupting gases, together with the inserted DBS$^-$ ions, will expand the crystal structure and give rise to the formation of the CoOOH nanosheets. The negative potential applied at the cathode side can lead to the generation of H$_2$ gases as confirmed by the bubbles produced at the cathode side during operation. The above process can be expressed as the following equations.

Anode:
$$LiCoO_2 \rightarrow Li_{1-\delta}CoO_2 + \delta Li^+ + \delta e^- \tag{1}$$

$$CoO_2 + \frac{1}{2}H_2O \rightarrow CoOOH + \frac{1}{4}O_2 \tag{2}$$

Cathode:
$$\delta H_2O + \delta e^- \rightarrow \frac{1}{2}\delta H_2 + \delta OH^- \tag{3}$$
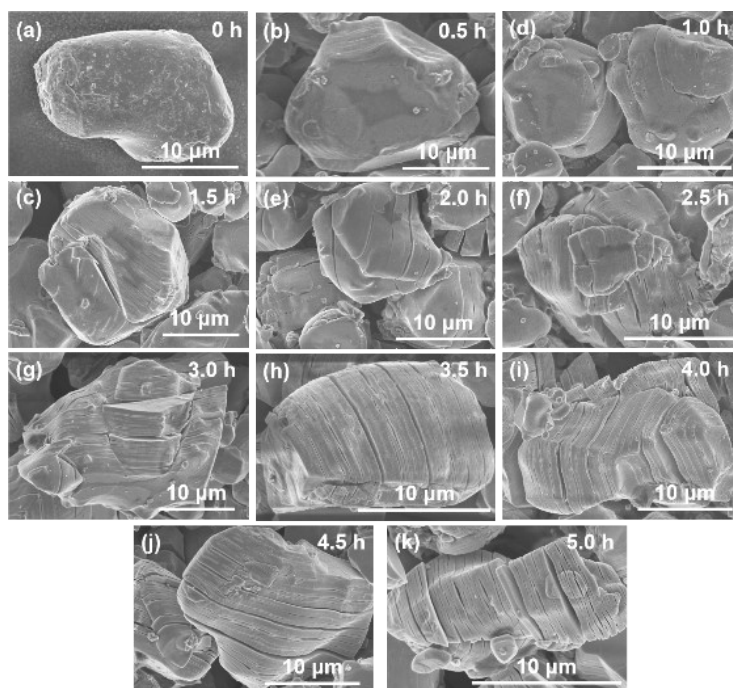
Fig. S3 SEM images of the intermediate products collected at different reaction time (at an interval of 30 min within 0-5 h).

The SEM results corresponding to the samples in Fig. 1a are displayed in Fig. S3. Starting from 4 h, obvious lamellar structures are observed for the samples. According to the typical sheet morphology of CoOOH, the above results further evidence the structural evolution of the samples during the exfoliation process.
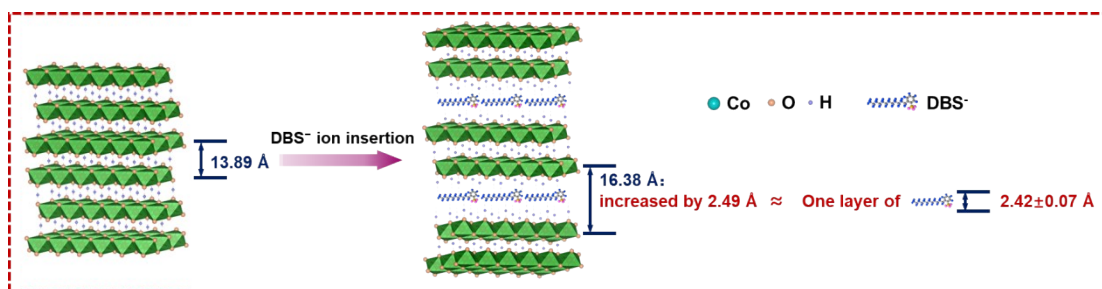
Fig. S4 Lattice expansion of CoOOH during the DBS⁻ insertion.

The similar value of the lattice spacing increase and the width of DBS⁻ anion suggests the insertion of one layer of DBS⁻ in between the adjacent CoO_x layers during the exfoliation process.
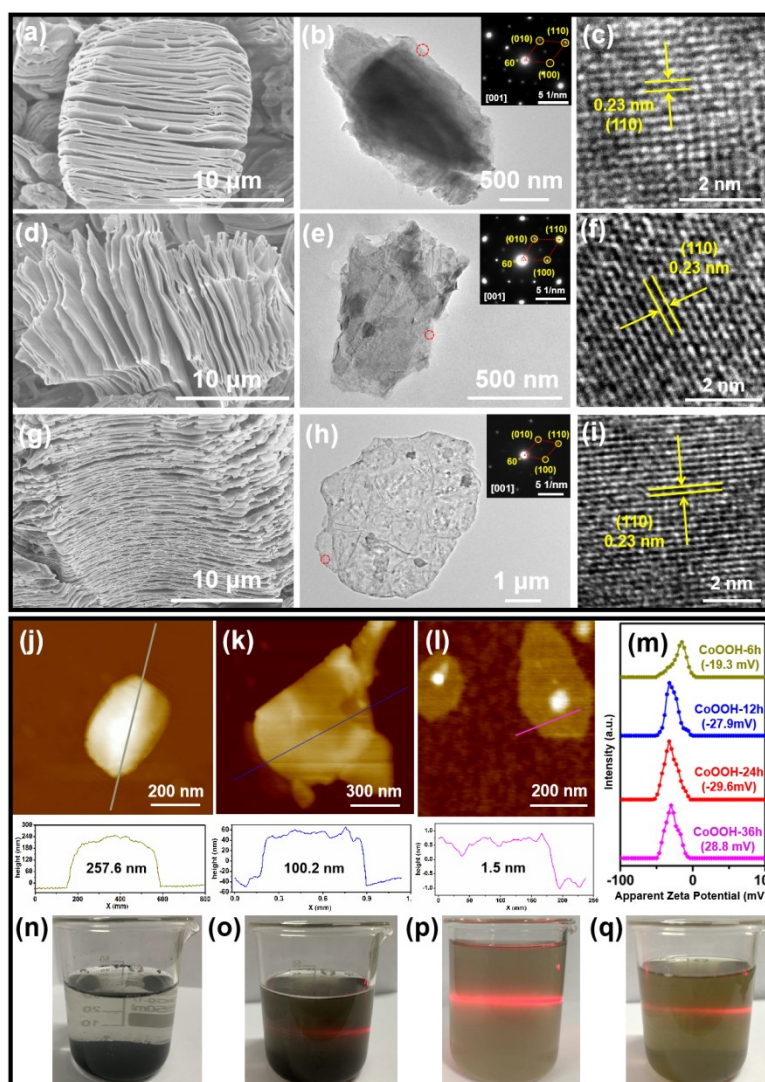
Fig. S5 (a) SEM image, (b) TEM image (inset: the corresponding SAED pattern), and (c) HRTEM image of CoOOH-6h. (d) SEM image, (e) TEM image (inset: the corresponding SAED pattern), and (f) HRTEM image of CoOOH-12h. (g) SEM image, (h) TEM image (inset: the corresponding SAED pattern), and (i) HRTEM image of CoOOH-36h. The height information of the (j) CoOOH-6h, (k) CoOOH-12h, (l) CoOOH-36h nanosheets obtained from AFM measurement. (m) Zeta potential of CoOOH samples. Optical images of (n) CoOOH-6h, (o) CoOOH-12h, (p) CoOOH-24h and (q) CoOOH-36h dispersed in water.

The SEM and TEM images of the CoOOH-6h, CoOOH-12h, and CoOOH-36h samples are depicted in Fig. S5. With the prolongation of the reaction time, the exfoliation of the bulk material into thinner sheets is observed. The SAED patterns (Fig. S5b, S5e, and S5h) and HRTEM images (Fig. S5c, S5f, and S5i) reveal these samples are correspond to CoOOH. The thicknesses of CoOOH-6h (Fig. S5j, 257.6 nm) and CoOOH-12h (Fig. S5k, 100.2 nm) are determined to be much larger than that of CoOOH-24h, attesting to the progressive two-step exfoliation process. Meanwhile, the comparative thickness value of CoOOH-36h (Fig. S5l, 1.5 nm) relative to that of CoOOH-24h corroborates that the exfoliation process reaches balanced at 24 h. The negative charge on the surface as well as the ultra-thin morphology of CoOOH-24h and CoOOH-36h give rise to the good stability of the nanosheets, which is manifested by the distinct Tyndall effect (Fig. S5p and S5q). In contrast, CoOOH-6h and CoOOH-12h tend to precipitate due to the thicker sheet morphology (Fig. S5n, and S5o).
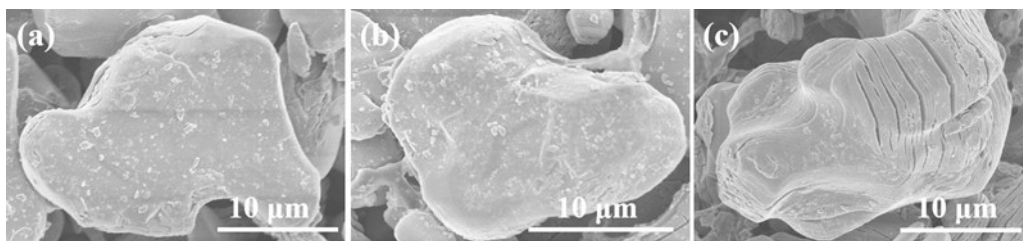
Fig. S6 SEM images of the electrochemically treated LiCoO$_2$ after applying a bias voltage of 0.25 V (a), 0.5 V (b) and 1.5 V (c), respectively for 24 h in SDBS solution.

As shown in Fig. S6c, LiCoO$_2$ can be exfoliated to some extent when 1.5 V is applied. Nevertheless, the exfoliation effects are not clearly observed in the control experiments where 0.25 V and 0.5 V are employed (Fig. S6a, and S6b). The phenomena can be due to that the applied voltages of 0.25 V and 0.5 V are lower than the required potential (~0.6-1.3 V *vs.* H$^+$/H$_2$) for the extraction of lithium ions from the structure, because of which the de-lithiation process is not able to be activated and the exfoliation of the materials is hindered.
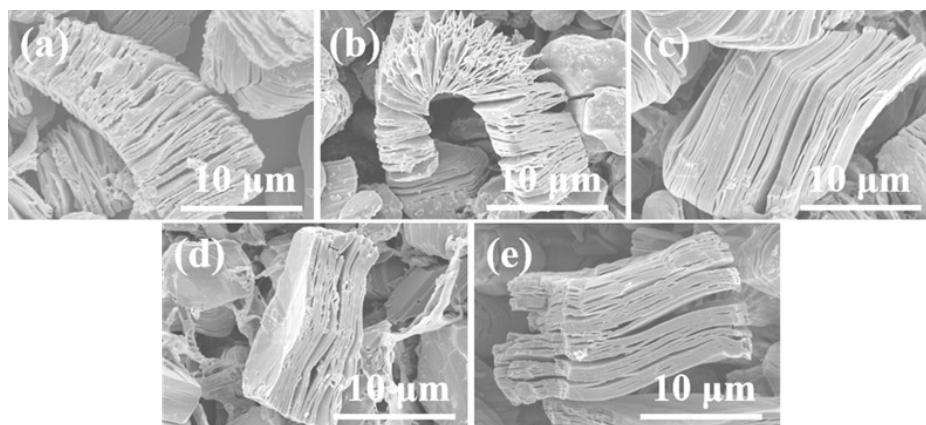
Fig. S7 SEM images of the electrochemically treated $LiCoO_2$ after applying a bias voltage of 3.0 V for 24 h in various electrolytes of (a) 0.5 M NaCl, (b) 0.5 M NH_4Cl, (c) 0.5 M KCl, (d) 0.2 M K_2SO_4, and (e) 0.2 M Na_2SO_4.

Other than SDBS, solutions of NaCl, NH_4Cl, KCl, K_2SO_4, and Na_2SO_4 were also studied, which all lead to inferior exfoliation effects as demonstrated in Fig. S7. The results attest to the importance of the introduction of DBS^- in the system. The role of DBS^- includes the insertion effects as well as the surface modification effects, *i.e.*, the anion surfactant of DBS^- can be strongly adsorbed on the surface of the layers and prevent the re-stacking of the neighboring nanosheets.
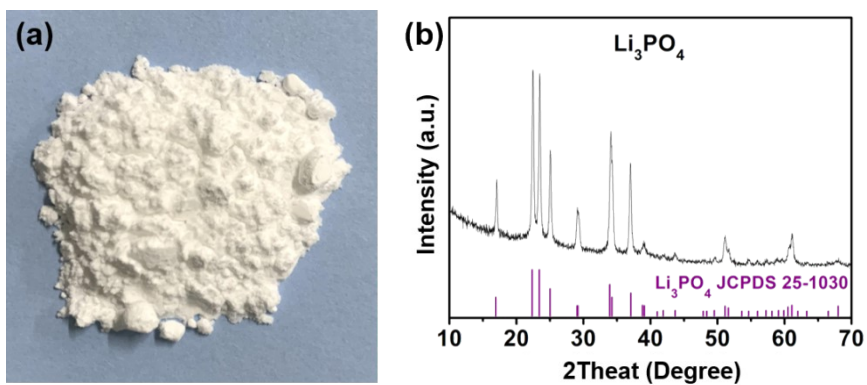
Fig. S8 (a) Photograph and (b) XRD pattern of the recycled Li₃PO₄ powders.

Accompanied by the exfoliation process, lithium ions in $LiCoO_2$ are extracted, which can be recovered in the form of Li_3PO_4 with the addition of H_3PO_4 solution (3 mol L^{-1}). Fig. S8a shows the photograph of the recycled Li_3PO_4 powder. The XRD pattern of the sample (Fig. S8b) can be well indexed to orthorhombic Li_3PO_4 (JCPDS 25-1030).
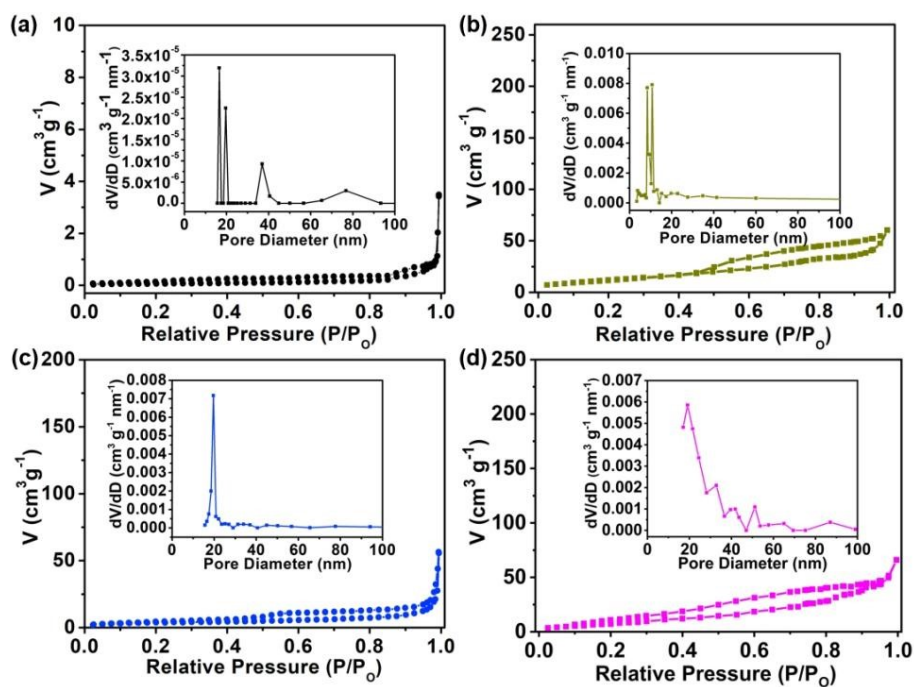
Fig. S9 N_2 adsorption/desorption isotherms of (a) the fresh $LiCoO_2$, (b) CoOOH-6h, (c) CoOOH-12h and (d) CoOOH-36h (inset: pore size distribution for the corresponding samples).

According to the N_2 adsorption/desorption isotherms of the samples (Fig. S9), the specific areas of CoOOH-36h, CoOOH-12h, CoOOH-6h, and the fresh $LiCoO_2$ are determined to be 46.348 m^2 g^{-1}, 30.672 m^2 g^{-1} and 19.153 m^2 g^{-1}, and 0.254 m^2 g^{-1}, respectively.
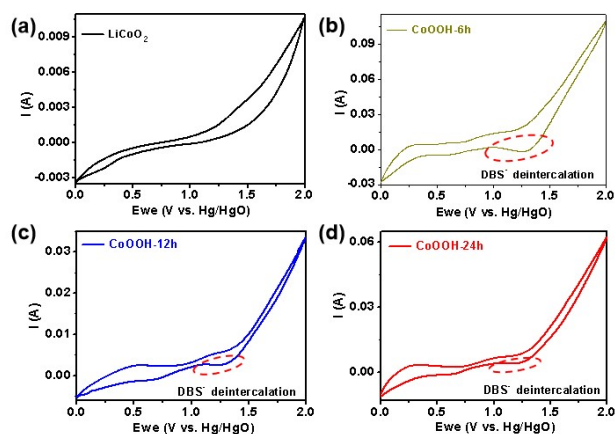
Fig. S10 CV curves of the (a) LiCoO$_2$, (b) CoOOH-6h, (c) CoOOH-12h, and (d) CoOOH-24h electrodes by using platinum foil as the counter electrode and Hg/HgO as the reference electrode.

The insertion of DBS$^-$ is further confirmed by cyclic voltammetry (CV) analysis. Specifically, the electrodes of CoOOH-6h, CoOOH-12h, CoOOH-24h, and the pristine LiCoO$_2$ were all investigated by CV analysis within the voltage range of 0 to 2 V (vs. Hg/HgO). Relative to the CV curve of the pristine LiCoO$_2$ (Fig. S10a), an additional cathodic peak is observed for all the exfoliated samples (marked with red circles, Fig. S10b, S10c, and S10d), which could be related to the deintercalation of DBS$^-$ anions. Moreover, with the extension of the exfoliation time, CoOOH is more exfoliated, which could lead to less inserted DBS$^-$ left in the structure (as the DBS$^-$ ions are released during exfoliation and washed out during purification). Such assumption is well in line with the CV results, as the intensities for the above peaks of the exfoliated samples follow the trend CoOOH-24h<CoOOH-12h<CoOOH-6h. Hence, the above results further evidence the insertion of DBS$^-$ in the exfoliated samples.

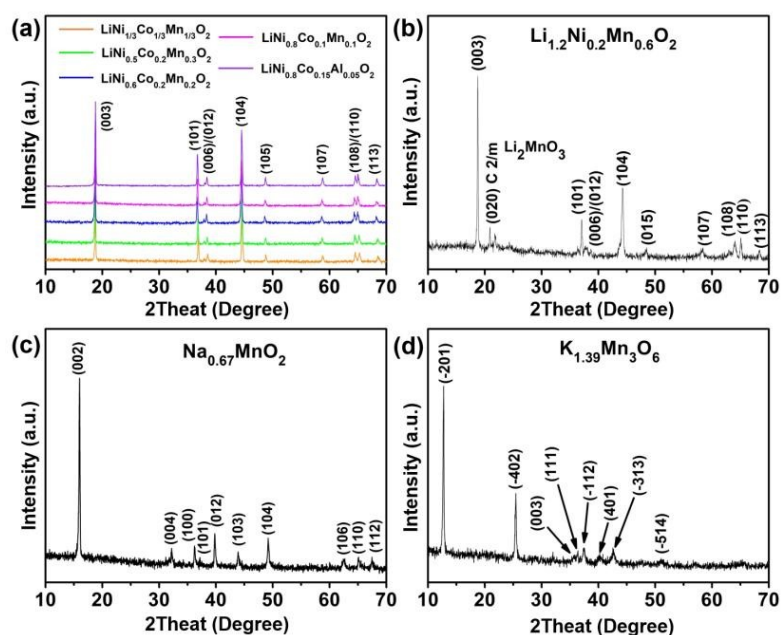**Fig. S11** XRD patterns of (a) $LiNi_{1/3}Co_{1/3}Mn_{1/3}O_2$, $LiNi_{0.5}Co_{0.2}Mn_{0.3}O_2$, $LiNi_{0.6}Co_{0.2}Mn_{0.2}O_2$, $LiNi_{0.8}Co_{0.1}Mn_{0.1}O_2$, and $LiNi_{0.8}Co_{0.15}Al_{0.05}O_2$, (b) $Li_{1.2}Ni_{0.2}Mn_{0.6}O_2$, (c) $Na_{0.67}MnO_2$, and (d) $K_{1.39}Mn_3O_6$.

Fig. S11a shows the XRD patterns of the layered ternary cathode materials. The strong peaks for all the samples can be well indexed to the α-NaFeO$_2$ structure with the R**Error!**m space group. Fig. S11b illustrates the XRD pattern of the as-prepared $Li_{1.2}Ni_{0.2}Mn_{0.6}O_2$, which can be indexed to the a-NaFeO$_2$ structure with the R**Error!**m space group. The weak peaks found at around 20-25º can be ascribed to a monoclinic system (C2/m space group) of Li_2MnO_3 phase. Fig. S11c presents the XRD pattern of the $Na_{0.67}MnO_2$. All the peaks can be indexed to the hexagonal system with the P63/mcm space group. Fig. S11d shows XRD reflections of the as-synthesized $K_{1.39}Mn_3O_6$. All the characteristic peaks match well with the monoclinic $K_{1.39}Mn_3O_6$ with space group C2/m.
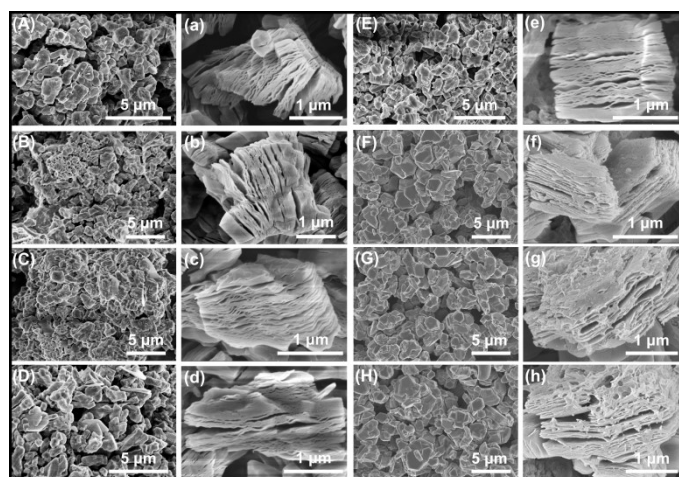
13

Fig. S12 SEM images of the exfoliated samples derived from (A) $LiNi_{1/3}Co_{1/3}Mn_{1/3}O_2$, (B) $LiNi_{0.5}Co_{0.2}Mn_{0.3}O_2$, (C) $LiNi_{0.6}Co_{0.2}Mn_{0.2}O_2$, (D) $LiNi_{0.8}Co_{0.1}Mn_{0.1}O_2$, (E) $LiNi_{0.8}Co_{0.15}Al_{0.05}O_2$, (F) $Li_{1.2}Ni_{0.2}Mn_{0.6}O_2$, (G) $Na_{0.67}MnO_2$, and (H) $K_{1.39}MnO_6$ after the electrochemical treatment for 6 h. SEM images of the exfoliated samples derived from (a) $LiNi_{1/3}Co_{1/3}Mn_{1/3}O_2$, (b) $LiNi_{0.5}Co_{0.2}Mn_{0.3}O_2$, (c) $LiNi_{0.6}Co_{0.2}Mn_{0.2}O_2$, (d) $LiNi_{0.8}Co_{0.1}Mn_{0.1}O_2$, (e) $LiNi_{0.8}Co_{0.15}Al_{0.05}O_2$, (f) $Li_{1.2}Ni_{0.2}Mn_{0.6}O_2$, (g) $Na_{0.67}MnO_2$, and (h) $K_{1.39}MnO_6$ after the electrochemical treatment for 24 h.

After applying a 3.0 V voltage for only 6 h, the intact structures of the original ternary LIBs cathode materials are all seriously destroyed and subtle cracks can be observed on the surfaces, but the exfoliation effects are yet very limited (Fig. S12A-E). For $Li_{1.2}Ni_{0.2}Mn_{0.6}O_2$, $Na_{0.67}MnO_2$, and $K_{1.39}MnO_6$ (Fig. S12F-H), the particles remain intact, except for some subtle cracks observed on the surfaces. After the electrochemical treatment for 24 h, these layered samples can be all successful exfoliating into thinner sheets, as displayed in Fig. S12a-h.
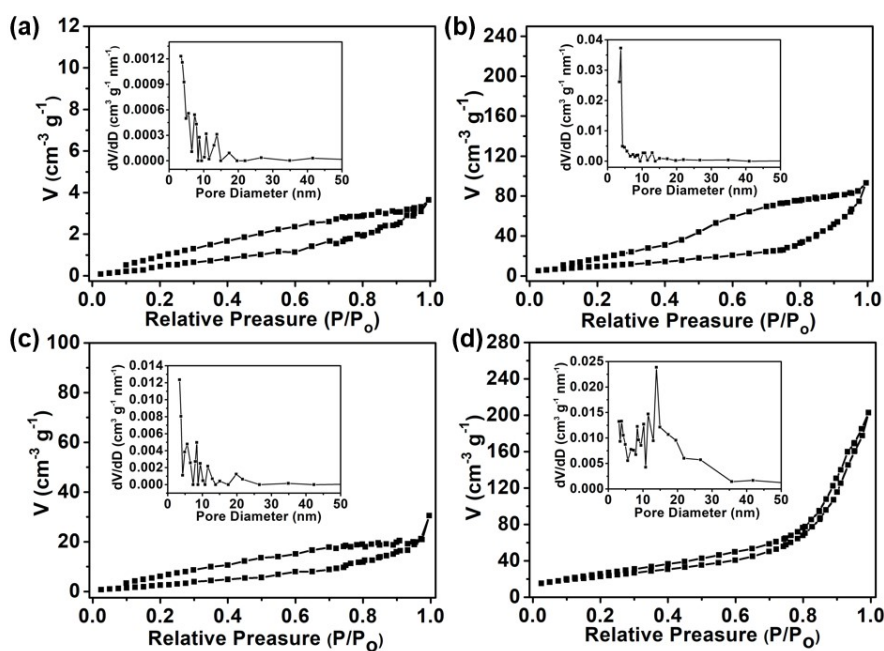
Fig. S13 N_2 adsorption/desorption isotherms and the corresponding pore size distribution plots of (a) the original $LiNi_{1/3}Co_{1/3}Mn_{1/3}O_2$ and (b) the exfoliated $LiNi_{1/3}Co_{1/3}Mn_{1/3}O_2$. N_2 adsorption/desorption isotherms and the corresponding pore size distribution plots of (c) the original $Na_{0.67}MnO_2$ and (d) the exfoliated $Na_{0.67}MnO_2$.

The N_2 gas sorption results shown in Fig. S13a and S13b reveal that the surface area is significantly enhanced from 2.827 $m^2\ g^{-1}$ for the original $LiNi_{1/3}Co_{1/3}Mn_{1/3}O_2$ to 109.054 $m^2\ g^{-1}$ for the nanosheet obtained after exfoliation for 24 h. Meanwhile, the surface area is significantly increased from 21.032 $m^2\ g^{-1}$ (Fig. S13c) for the original $Na_{0.67}MnO_2$ to 90.925 $m^2\ g^{-1}$ (Fig. S13d) for the nanosheet obtained after exfoliation for 24 h. These results clarifying the successful exfoliation of the bulk material into 2D nanostructure that possesses larger exposed surface.
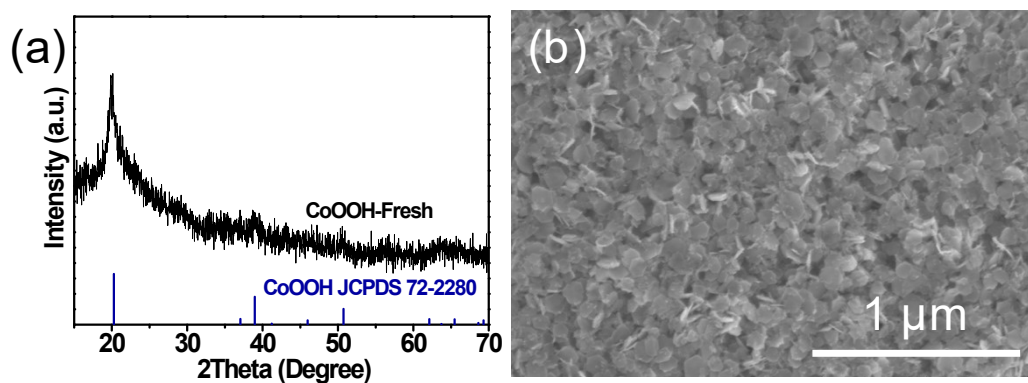
Fig. S14 (a) XRD pattern and (b) SEM image of CoOOH nanosheets (CoOOH-Fresh) prepared from fresh reagents.

CoOOH nanosheets were also prepared using fresh reagents. XRD reflections of the as-obtained sample can be indexed to CoOOH (PDF #72-2280), while the SEM image corroborates its sheet morphology.
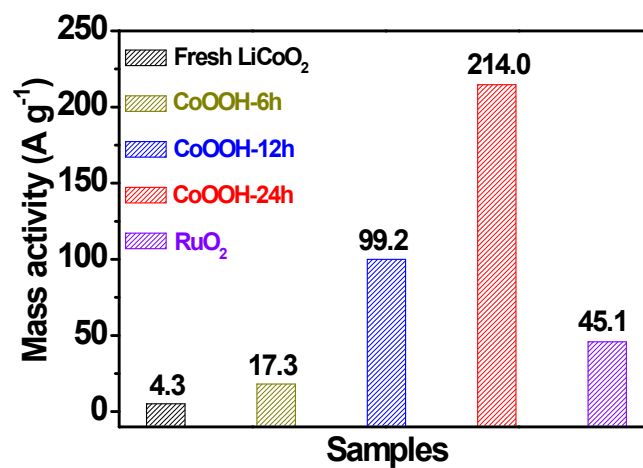
Fig. S15 Mass activities of fresh $LiCoO_2$, CoOOH-6h, CoOOH-12h, CoOOH-24h, and RuO_2 evaluated at 1.60 V vs. RHE.

The mass activities of $LiCoO_2$, CoOOH-6h, CoOOH-12h, CoOOH-24h, and RuO_2 were investigated at 1.60 V vs. RHE. The results reveal that the mass activity of CoOOH-24h reaches 214.0 A g^{-1}, which is higher than 4.3 A g^{-1}, 17.3 A g^{-1}, 99.2 A g^{-1}, and 45.1 A g^{-1} obtained for $LiCoO_2$, CoOOH-6h, CoOOH-12h, and RuO_2, respectively.

	Overpotentials at 10 mA cm⁻²	Mass activity at 1.60 V vs. RHE
NH₄Cl	408 mV	12.39 A g⁻¹
Na₂SO₄	407 mV	14.79 A g⁻¹
NaCl	367 mV	35.93 A g⁻¹
K₂SO₄	395 mV	17.47 A g⁻¹
KCl	383 mV	23.72 A g⁻¹
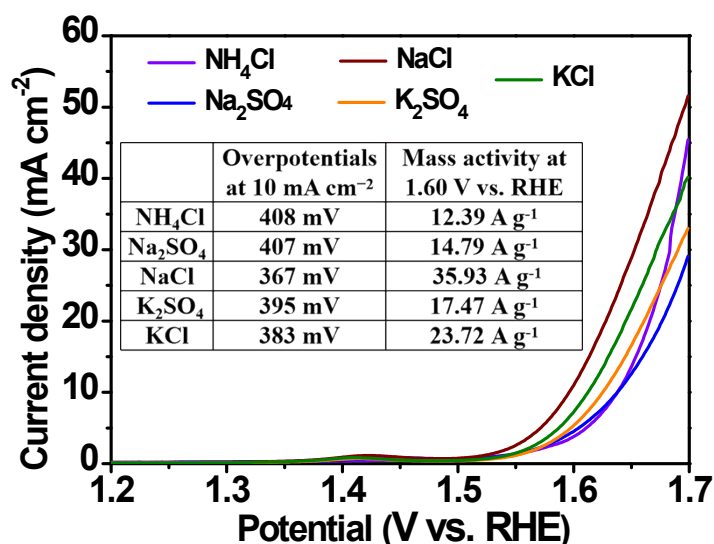
Fig. S16 Polarization curves of the electrochemically treated $LiCoO_2$ after applying a bias voltage of 3.0 V for 24 h in various electrolytes.

Except for exfoliation time, the OER catalytic performances of the CoOOH samples could be also related to the electrolytes applied during synthesis, which are further investigated. As shown in Fig. S16, when using electrolytes of NH_4Cl, NaCl, Na_2SO_4, K_2SO_4, and KCl, the as-obtained samples all exhibit inferior catalytic activities (at 10 mA cm⁻²) and mass activities (at 1.60 V vs. RHE) relative to CoOOH-24h. The results corroborate the significant role of SDBS in enhancing the OER performances of the electrochemically treated CoOOH samples, which could be correlated with the insertion effects of DBS^- that effectively lead to the exfoliation of the samples during synthesis.

Fig. S17 Cyclic voltammograms recorded for (a) LiCoO$_2$, (b) CoOOH-6h, (c) CoOOH-12h, and (d) CoOOH-24h at various scan rates.

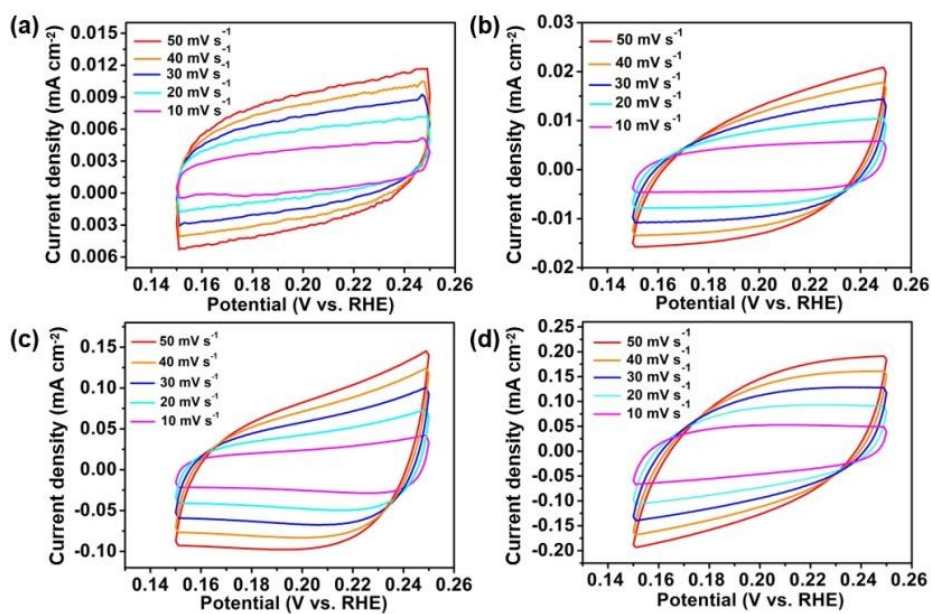Fig. S17 shows the cyclic voltammograms recorded for LiCoO$_2$, CoOOH-6h, CoOOH-12h, and CoOOH-24h at various scan rates, which are utilized to investigate the electrochemical active surface area (ECSA) of the samples.
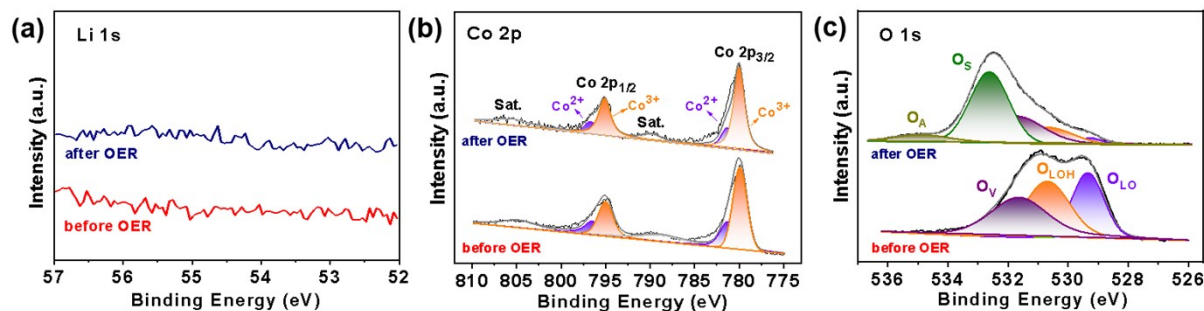
Fig. S18 High resolution XPS spectra of (a) Li 1s, (c) Co 2p, and (c) O 1s for CoOOH-24h before and after stability test for 65 h at 10 mA cm^{-2}.

XPS analyses of CoOOH-24h before and after the long-term stability test were carried out. The results reveal the absence of Li signal in the pristine CoOOH-24h (Fig. S18a), further confirming that the Li$^+$ ions are completely extracted from the structure. The Co 2p spectra of CoOOH-24h could be deconvoluted into the two components of Co^{3+} and Co^{2+} (Fig. S18b). Further analysis reveals that the relative ratio of Co^{2+}/Co^{3+} in CoOOH-24h collected after the long-term electrolysis test is lower than that of the pristine CoOOH-24 (decreased from 0.51 to 0.26). The results demonstrate that a proportion of Co^{2+} is oxidized to Co^{3+}, which could be induced by the fresh oxygen during the OER processes. Such phenomenon was also previously reported for other cobalt-based OER catalysts. Due to that Co-ions with higher valency have been verified to be more likely to become active sites, the Co-ions with increased valence state in CoOOH are expected to further benefit the OER catalysis during operation. The high-resolution O 1s spectrum shows two additional peaks in CoOOH-24h obtained after the electrolysis test when compared with that of the pristine CoOOH-24h sample. The appearance of the new signals may originate from the absorbed O-containing species during OER process.
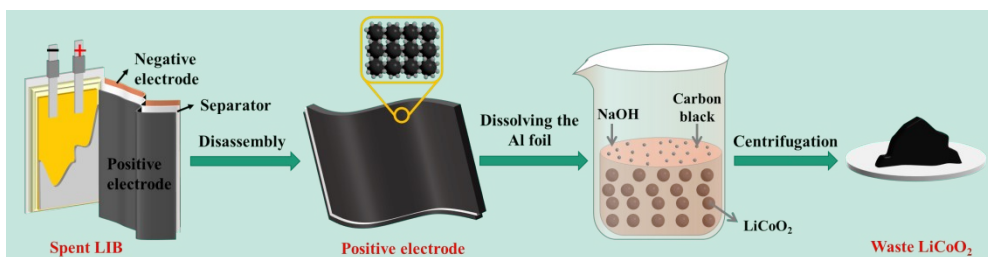
Fig. S19 Recycling process of spent LiCoO$_2$ powder.

The recycling process of the waste LiCoO$_2$ powders is shown in Fig. S19. In a typical collection of the waste electrode materials, a LIB in a spent mobile phone was fully discharged by immersing it in the NaCl solution to discharge completely. Next, the LIB was dismantled to remove the metallic and plastic components, after which the waste LiCoO$_2$ material could be easily separated from the negative electrode and the separators. The obtained positive electrode was then added into in the NaOH solution to peel off the waste cathode material from the Al current collector. After thoroughly rinsing with water and drying at 80 °C for 12 h, the spent LiCoO$_2$ powder can be collected.
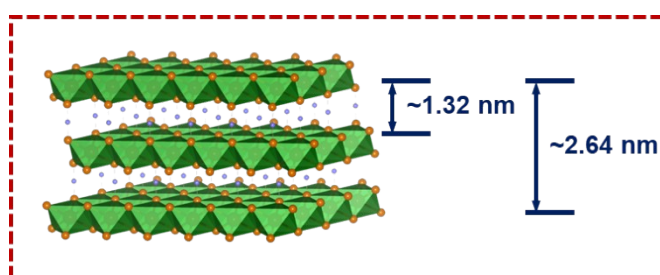
Fig. S20 Crystal structure of the CoOOH with triply stacked CoO$_x$ layers.

The morphological information obtained from the AFM measurements reveals that the thickness of the CoOOH nanosheet is around 3 nm, indicating that the CoOOH sample consists of triply stacked CoO$_x$ layers bridged by hydrogen bonding (Fig. S20).
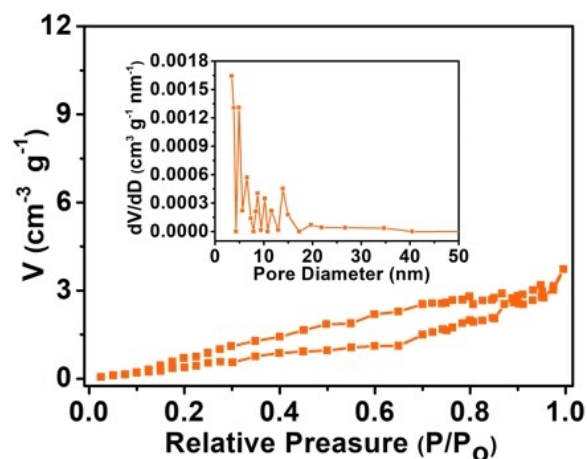
Fig. S21 N_2 adsorption/desorption isotherms and the corresponding pore size distribution plots of the spent $LiCoO_2$.

The N_2 gas sorption results shown in Fig. S21 reveal that the surface area is significantly enhanced from 3.132 m^2 g^{-1} for the spent $LiCoO_2$.
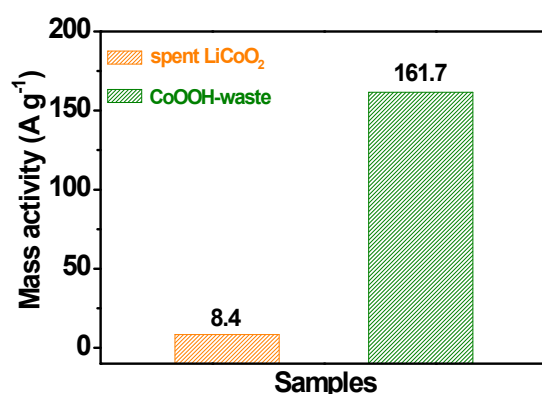
Fig. S22 Mass activities of spent $LiCoO_2$ and CoOOH-waste evaluated at 1.60 V vs. RHE.

The mass activity for the CoOOH-waste is 161.7 A g^{-1} at 1.60 V vs. RHE, which surpasses that of the spent $LiCoO_2$ (8.4 A g^{-1}), further corroborating the outstanding OER performance of the exfoliated CoOOH samples.

Table S1. ICP-MS analysis of the atomic ratios of Li and Co in the CoOOH-6h sample.

Sample	Li (ppb)	Co (ppb)	Atomic ratio of Li	Atomic ratio of Co
CoOOH-6h	116.3	176300	0.0055	0.9945

Table S2. Summary of the information obtained from the N_2 adsorption/desorption measurements.

Samples	Surface area ($m^2\ g^{-1}$)	Average pore size (nm)
CoOOH-6h	0.254	10.3
CoOOH-12h	19.153	19.5
CoOOH-24h	45.114	19.8
CoOOH-36h	46.348	24.4

Table S3. The relative ratio of Co^{2+}/Co^{3+} obtained by the peak area ratio of XPS.

Samples	The relative ratio of Co^{2+}/Co^{3+}
$LiCoO_2$	0.22
CoOOH-6h	0.83
CoOOH-12h	0.60
CoOOH-24h	0.51

Table S4. The relative ratio of oxygen vacancy (O_V) in samples.

Samples	The relative ratio of O_V
$LiCoO_2$	0.17
CoOOH-6h	0.56
CoOOH-12h	0.39
CoOOH-24h	0.33

Table S5. ICP-MS analysis of the atomic ratios of Li, Na, K, Ni, Co, Mn, Al in the $LiNi_{1/3}Co_{1/3}Mn_{1/3}O_2$, $LiNi_{0.5}Co_{0.2}Mn_{0.3}O_2$, $LiNi_{0.6}Co_{0.2}Mn_{0.2}O_2$, $LiNi_{0.8}Co_{0.1}Mn_{0.1}O_2$, $LiNi_{0.8}Co_{0.15}Al_{0.05}O_2$, $Li_{1.2}Ni_{0.2}Mn_{0.6}O_2$, $Na_{0.67}MnO_2$, and $K_{1.39}Mn_3O_6$ samples.

Samples	Concentration ($\times 10^3$ ppb)							Measured atomic ratio
	Li	Na	K	Ni	Co	Mn	Al	
$LiNi_{1/3}Co_{1/3}Mn_{1/3}O_2$	20.59			56.25	57.37	52.91		Li:Ni:Co:Mn = 1.03:0.33:0.34:0.34
$LiNi_{0.5}Co_{0.2}Mn_{0.3}O_2$	10.46			66.67	25.49	40.56		Li:Ni:Co:Mn = 1.06:0.50:0.19:0.32
$LiNi_{0.6}Co_{0.2}Mn_{0.2}O_2$	30.78			150	49.47	48.48		Li:Ni:Co:Mn = 1.04:0.60:0.22:0.23
$LiNi_{0.8}Co_{0.1}Mn_{0.1}O_2$	20.58			131.9	16.68	16.29		Li:Ni:Co:Mn = 1.06:0.80:0.10:0.11
$LiNi_{0.8}Co_{0.15}Al_{0.05}O_2$	19.75			126.7	21.54		3.398	Li:Ni:Co:Al = 1.05:0.80:0.14:0.05
$Li_{1.2}Ni_{0.2}Mn_{0.6}O_2$	80.25			105.2		302.3		Li:Ni:Mn= 1.26:0.21:0.60
$Na_{0.67}MnO_2$		35.42				129.5		Na:Mn=0.65:1
$K_{1.39}Mn_3O_6$			92.32			96.36		K:Mn=1.35:3

Table S6. Gibbs free energy of the three OER intermediates (V_o, *O, *OH, *OOH, V_o+O_2) for bulk $LiCoO_2$, bulk CoOOH, and CoOOH nanosheets with different contents of oxygen vacancies. The Gibbs free energy differences (ΔG) for each elementary steps can be calculated by the following formulas:

$$\Delta G_1 = G_{*O} - G_{V_0} \qquad\qquad\qquad 1$$

$$\Delta G_2 = G_{*OH} - G_{*O} \qquad\qquad\qquad 2$$

$$\Delta G_3 = G_{*OOH} - G_{*OH} \qquad\qquad\qquad 3$$

$$\Delta G_4 = G_{V_0+O_2} - G_{*OOH} \qquad\qquad\qquad 4$$

Bulk $LiCoO_2$ with 1/9 ML O_v concentrations		Bulk CoOOH with 1/9 ML O_v concentrations	
V_o	0 eV	V_o	0 eV
*O	0.42 eV	*O	0.68 eV
*OH	1.48 eV	*OH	2.34 eV
*OOH	3.46 eV	*OOH	4.03 eV
$V_o + O_2$	4.92 eV	$V_o + O_2$	4.92 eV
ΔG_1	0.42 eV	ΔG_1	0.72 eV
ΔG_2	1.06 eV	ΔG_2	1.65 eV
ΔG_3	1.98 eV	ΔG_3	1.74 eV
ΔG_4	1.46 eV	ΔG_4	0.81 eV

CoOOH nanosheets	with 1/9 ML O_v concentrations	with 1/3 ML O_v concentrations	with 2/3 ML O_v concentrations
Vo	0 eV	0 eV	0 eV
*O	0.68 eV	0.46 eV	-0.22 eV
*OH	2.34 eV	1.88 eV	0.84 eV
*OOH	4.03 eV	3.68 eV	3.28 eV
Vo +O_2	4.92 eV	4.92 eV	4.92 eV
ΔG_1	0.68 eV	0.46 eV	-0.22 eV
ΔG_2	1.66 eV	1.42 eV	1.06 eV
ΔG_3	1.69 eV	1.80 eV	2.44 eV

| ΔG_4 | 0.89 eV | 1.24 eV | 1.64 eV |

Table S7. OER activities of the CoOOH nanosheets developed in this work in comparison with some of the most advanced OER catalysts reported in literatures.

Electrocatalysts	η at 10 mA cm^{-2} (mV)	Tafel slope (mV dec^{-1})	Reference
CoOOH-6h	394	62.7	
CoOOH-12h	326	68.8	
CoOOH-24h	301	53.8	**This work**
CoOOH-waste	306	52.5	
FeCoOOH nanosheets	252	61.8	1
Co_3O_4 /HNCP-40	333	69	2
CoOOH HNSs	305	63	3
$Co_{0.89}Ca_{0.11}$-CPs	371	58.3	4
CoOOH/NF	370	83	5
CeO_x/CoO_x	313	66	6
$Co_2Mo_3O_8$@NC-800	331	87.5	7
CoS_x	330	62	8
LC-CoOOH NAs/CFC	294	70.73	9
$FeCo_2Ni$-MOF-74	254	21.4	10
Mn-CoP porous nanosheets	288	77.2	11
Co,Nb-MoS_2/TiO_2 HSs	260.1	65.0	12

References

1   J. Q. Lv, X. F. Guan, Y. Y. Huang, L. X. Cai, M. X. Yu, X. Y. Li, Y. L. Yua and D. G. Chen, *Nanoscale*, **2021**, *13*, 15755-15762.

2   D. Ding, K. Shen, X. Chen, H. Chen, J. Chen, T. Fan, R. Wu, Y. Li, *ACS Catal.,* **2018**, *8*, 7879-7889.

3   Q. L. Hong, Q. G. Zhai, X. L. Liang, Y. Yang, F. M. Li, Y. C. Jiang, M. C. Hu, S. N. Li and Y. Chen, *J. Mater. Chem. A,* **2021**, *9*, 3297-3302.

4   P. Su, S. Ma, W. Huang, Y. Boyjoo, S. Bai, and J. Liu, *J. Mater. Chem. A,* **2019**, *7*, 19415-19422.

5   P. Chen, T. Zhou, S. Wang, N. Zhang, Y. Tong, H. Ju, W. Chu, C. Wu, and Y. Xie, *Angew. Chem. Int. Ed.,* **2018**, *57*, 15471-15476.

6   J. Kim, K. Shin, K. Kawashima, D. H. Youn, J. Lin, T. E. Hong, Y. Liu, B. R. Wygant, J. Wang, G. Henkelman, and C. B. Mullins, *ACS Catal.,* **2018**, *8*, 4257-4265.

7   T. Ouyang, X. Wang, X. Mai, A. Chen, Z. Tang, and Z. Liu, *Angew. Chem. Int. Ed.,* **2020**, *59*, 11948-11957.

8   K. Fan, H. Zou, Y. Lu, H. Chen, F. Li, J. Liu, L. Sun, L. Tong, M. F. Toney, M. Sui, and J. Yu, *ACS Nano*, **2018**, *12,* 12369-12379.

9   S. H. Ye, J. P. Wang, J. Hu, Z. D. Chen, L. R. Zheng, Y. H. Fu, Y. Q. Lei, X. Z. Ren, C. X. He, Q. L. Zhang, and J. H. Liu, *ACS Catal.*, **2021**, *11*, 6104-6112.

10 X. Q. Mu, H. M. Yuan, H. Y. Jing, F. J. Xia, J. S. Wu, X. Y. Gu, C. Y. Chen, J. C. Bao, S. Liu, and S. C. Mu, *Applied Catalysis B: Environmental*, **2021**, *296*, 120095.

11 Y. H. Liu, N. Ran, R. Y. Ge, J. J. Liu, W. X. Li, Y. Y. Chen, L. Y. Feng, and R. C. Che, *Chem. Eng. J.*, **2021**, *425*, 131642.

12 D. C. Nguyen, T. L. L. Doan, S. Prabhakaran, D. T. Tran, D. H. Kim, J. H. Lee, and N. H. Kim, *Nano Energy*, **2021**, *82*, 105750.